Int J Adv Manuf Technol (2017) 88:1075–1087
DOI 10.1007/s00170-016-8830-y

ORIGINAL ARTICLE

Understanding the temperature distribution and influencing factors during high-frequency induction brazing of CBN super-abrasive grains

Wei Xu[1] · Wenfeng Ding[1] · Yejun Zhu[1] · Xin Huang[1] · Yucan Fu[1]

Received: 14 February 2016 / Accepted: 25 April 2016 / Published online: 5 May 2016

Abstract The temperature distribution characteristics in high-frequency induction brazing of cubic boron nitride (CBN) super-abrasive grains is investigated based on finite element simulation in this article. Influences of the following factors, i.e., current frequency, current magnitude, heating gap, and scanning speed, on the resultant heating temperature are discussed. The results obtained display that, during the rotating induction heating process, the effective heating zone is concentrated on the top surface of the metallic wheel substrate (i.e., AISI 1045 steel) below the coil. The highest value of the resultant heating temperature becomes larger when heating with a higher current frequency, a higher current magnitude, and smaller heating gap values; however, a higher peripheral scanning speed results in a decrease of the resultant highest temperature. The optimum parameters are determined as the heating gap of 2 mm, current frequency of 1 MHz, current magnitude of 20 A, and peripheral scanning speed of 0.5 mm/s. Finally, the simulation results are testified and validated in the high-frequency induction brazing experiment of CBN grains.

Keywords High-frequency induction brazing · Finite element simulation · Temperature distribution · Optimum parameters · Metallic wheel substrate

✉ Wenfeng Ding
dingwf2000@vip.163.com

[1] College of Mechanical and Electrical Engineering, Nanjing University of Aeronautics and Astronautics, Nanjing 210016, People's Republic of China

1 Introduction

Because a precision brazing process at elevated temperatures could build a chemical bridge between cubic boron nitride (CBN) super-abrasive grains and metallic wheel substrate with the help of an Ag-Cu-Ti filler alloy, higher bonding strength to grains has been the primary advantage of a brazed CBN wheel, which makes that the monolayer brazed CBN super-abrasive wheels have been reported to outperform their electroplated and vitrified-bonded counterparts [1–3]. For this reason, in the recent years, the monolayer brazed CBN wheels have shown a great potential in grinding titanium alloy and nickel-based superalloy, which are broadly regarded as difficult-to-cut materials [4–11].

As for the current fabrication techniques of brazed CBN wheels, three thermal sources have been utilized to heat the metallic wheel substrate (i.e., AISI 1045 steel materials) and Ag-Cu-Ti filler alloy, including vacuum resistance furnace, laser, and high-frequency induction. Surely, each thermal source has its own characteristics and advantages. For example, as for the high-frequency induction brazing, it has the great advantages of rapid heating rate and locally heating. Particularly, it is more suitable to fabricate the brazed CBN wheels with large size (i.e., 400 mm in diameter) due to the fact that the large wheel could not be brazed in the vacuum resistance furnace because of the limited chamber size and significant deformation of the metallic wheel substrate, and the quality control of the laser brazing is complex and also very difficult.

It is noted that, however, there still exist some problems when fabricating the brazed CBN wheels based on high-frequency induction heating technique [12], the reason of which is due to the insufficient understanding of the heating

temperature distribution [13]. Under such condition, the temperature control and heating parameter optimization could not be conducted well, which resulted in the bad joining among the metallic wheel substrate, Ag-Cu-Ti filler alloy and CBN super-abrasive grains [14]. Therefore, it is necessary to deeply understand the temperature distribution and influencing factors during high-frequency induction brazing of CBN grains.

Experimental detection is still an important method to study the temperature distribution in induction heating. For instance, Codrington et al. [15] developed the high temperature measuring equipment, with which the thermocouples are used to measure the heating temperature and provide a feedback signal for PID control of the induction heater. Jang et al. [16] applied the thermocouples and infrared thermal imaging system, respectively, to measure comparatively the temperatures at the inside and outside surface of a steel hollow cylinder during the induction heating process. Franco et al. [17] proposed an infrared sensor and detected the real-time temperature evolution. However, all the reported experimental techniques could merely measure the temperature at one point or at a rather local zone within the induction-heating zone, and cannot characterize the temperature distribution within the whole brazing zone.

In fact, besides the experimental method, the finite element (FE) simulation method has also been broadly applied to investigate quantitatively the temperature distribution in the current heating analysis. Chen et al. [18] established a FE model of a 2-inch. SiC growth system and investigated the effects of induction heating parameters on temperature distribution. Mei et al. [19] proposed a heat-generating rate model of slab in induction heating from a hot rolling plant, and the temperature evolution of slab was solved by the developed FE code. Zhang et al. [20] established a thermo-mechanical 3D-FE model for preheating and heat bending of large-diameter thin-walled commercial pure titanium tube in terms of both accuracy and efficiency, and temperature distribution of bending tools was predicted by the developed preheating model.

For the abovementioned reason, a finite element simulation is used to characterize and understand the temperature distribution in the high-frequency heating system of brazing CBN grains in the present work. The effects of some key influencing factors on the resultant temperature are investigated. At the same time, experimental measurement is also carried out to testify the simulation results. All these have a significant meaning in further optimizing and controlling the induction heating parameters in brazing CBN grains; as such, good machining performance of monolayer brazed CBN super-abrasive wheels could be provided.

2 Finite element model for simulating temperature distribution during high-frequency induction heating

2.1 Numerical simulations principle

Since the properties of heated materials are temperature dependent, the induction heating process may be considered as the coupling of steady-state alternating current (AC) electromagnetic field and transient temperature field. The heated material surface is in the AC electromagnetic field, and the induced eddy current field is accordingly produced. The material surface is heated by the internal heat source, which comes from the induced eddy current field. Under such condition, the simulation analysis should include both the electromagnetic field and the temperature field, in which the electromagnetic field is governed by Maxwell's equations, and its differential form could be described as follows [21]:

$$\begin{cases} \nabla \times \vec{H} = \vec{J} + \dfrac{\partial \vec{D}}{\partial t} \\ \nabla \times \vec{E} = -\dfrac{\partial \vec{B}}{\partial t} \\ \nabla \cdot \vec{B} = 0 \\ \nabla \cdot \vec{D} = \rho_e \end{cases} \tag{1}$$

where $\vec{E}$ is the electric field intensity vector (V/m or N/C); $\vec{H}$ is the magnetic field intensity vector (A/m); $\vec{A}$ is the conduction current density vector (A/m^2); $\vec{D}$ is the electric flux density vector (C/m^2); $\vec{B}$ is the magnetic flux density vector (T or N/(A·m)); ρ_e is the electric charge density (C/m^3).

The field variables have the relational expressions as follows [22]:

$$\begin{cases} \vec{J} = \sigma \vec{E} \\ \vec{B} = \mu \vec{H} \end{cases} \tag{2}$$

where μ is the relative magnetic permeability (H/m); σ is the electrical conductivity (S/m).

In order to solve Eq. (1), a magnetic vector potential $\vec{A}$ and an electric scalar potential φ are brought into as follows:

$$\vec{B} = \nabla \times \vec{A} \tag{3}$$

$$\vec{E} = -\nabla\varphi - \frac{\partial \vec{A}}{\partial t} \tag{4}$$

Differential form of Maxwell's equations is solved by a comprehensive analysis of the above equations. Considering the following:

$$\nabla \times \left(\frac{\nabla \times \vec{A}}{\mu} \right) + \sigma \left(\frac{\partial \vec{A}}{\partial t} + \nabla\varphi \right) = 0 \tag{5}$$

where $\vec{A}$ is the magnetic vector potential (Wb/m); φ is the electric scalar potential (V).

The basic equations of the transient temperature field are specified as follows:

$$\vec{\varphi} = -\lambda \nabla \vec{T} \tag{6}$$

$$\nabla \cdot \vec{\varphi} + C_v \frac{\partial T}{\partial t} = q_v \tag{7}$$

where $\vec{\varphi}$ is the heat flux density vector (W/m^2).

The final temperature field equation is solved, given as follows [23, 24]:

$$\nabla\left(-\lambda \nabla \vec{T}\right) + C_v \frac{\partial T}{\partial t} = q_v = \rho \left|\vec{J}\right|^2 \tag{8}$$

where T is the temperature on the heated materials surface; C_v is the volume heat capacity (J/(m^3·K)); q_v is the internal heat source density (A/m^2).

In the present investigation, the finite element simulation processes in a time increment step are clarified as follows: firstly, solve the eddy current field based on the initial temperature condition; secondly, use the eddy current field to calculate the heat, and determine the temperature field based on thermal analysis; thirdly, update the heated workpiece material properties with temperature, and recalculate the temperature in the next time increment step.

2.2 Geometry modeling and meshes

The two-dimensional (2D) model of a high-frequency induction heating system applied in this work is displayed in Fig. 1a. The monolayer brazed CBN super-abrasive wheel is composed of a commercial AISI 1045 steel substrate, Ag-Cu-Ti filler alloy and CBN grains. Particularly, the filler alloy and CBN grains spread uniformly on the top surface of the metallic wheel substrate, as shown in Fig. 1b. The inductor, above the CBN wheel, consists of a trough-type magnetizer and a coil. The magnetizer material is Ferrotron 559H. The coil is made from a rectangular copper tube with good electrical conductivity, and the cooling water flows through it for keeping the coil at a low temperature.

The external and internal diameters of the wheel substrate are 400 and 127 mm, respectively; meanwhile, the width of the wheel outer circumference, that is, the width of the heated top surface of wheel substrate is 12 mm. The cross-section diagram of the inductor is schematically displayed in Fig. 1b, in which the coil is in a size of 3 mm × 2 mm and the magnetizer is in a size of 9 mm × 12 mm. The thickness of the coil is 0.5 mm.

Considering the finite element model established is two dimensions, the electromagnetic edge effect [25] is not considered in the current simulation work. Additionally, because the eddy current only occurs at the surface of the heated part of the metallic wheel substrate, the heat produced in the induction heating only exists on the metallic wheel substrate, while the heat transfers from the metallic wheel substrate to the CBN grains and Ag-Cu-Ti filler alloy, which makes the filler alloy melt smoothly. Therefore, the CBN grains and Ag-Cu-Ti filler alloy have no influence on the temperature distribution during induction heating. Under such condition, a simplification of the induction heating model without the CBN grains and Ag-Cu-Ti alloy could be made, as the finite element model shown in Fig. 2.

Figure 2a shows the meshes of the whole finite element model, which is mainly meshed with the triangular elements. The outer regions including the wheel substrate and the inductor are infinite box and inner air, and the sizes of the internal and external diameters are 1000 and 1200 mm, respectively. The local heating regions are illustrated in Fig. 2b. The red section is the coil with a hollow structure, while the yellow section covering the wheel is compressible air. The mesh of the heated wheel substrate surface contains two quadrangular elements in the skin depth. The heating zone is meshed by the thin grid with the smallest line element of 0.2 mm. The skin depth is 0.55 mm in the case of the heating temperature of 1000 °C during induction heating [26]. When the heating gap is 2 mm, 145011 nodes and 70422 triangular elements are contained in the whole mesh.

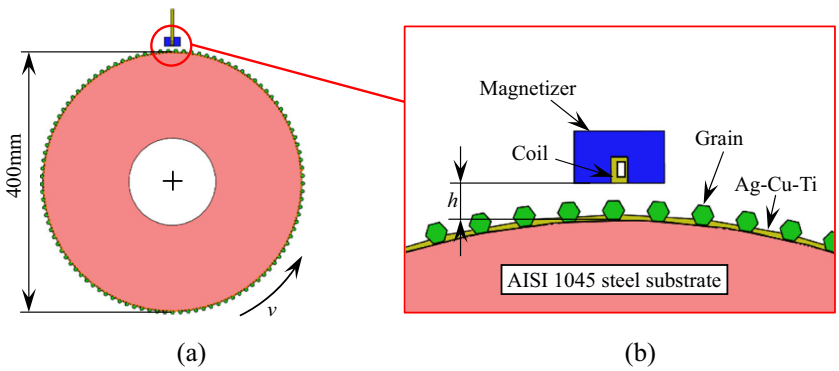

Fig. 1 Geometry model of high-frequency induction heating system.**a** Whole geometry model. **b** The inductor and heated wheel surface

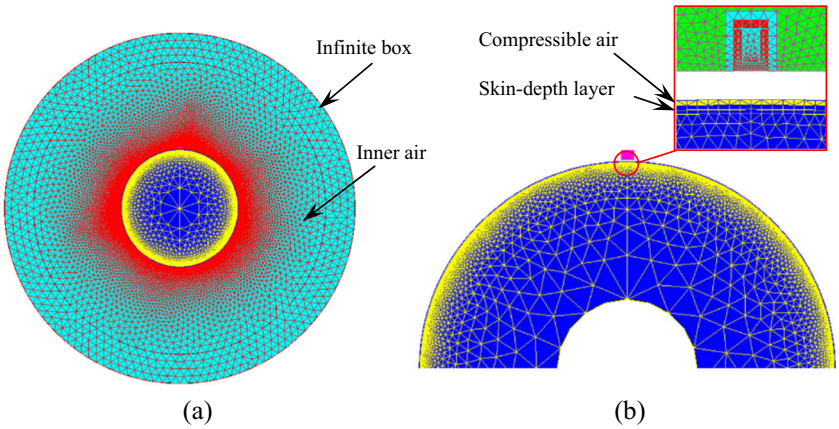

Fig. 2 Meshing of the finite element model. **a** Meshing of the whole model. **b** Meshing of the coil and wheel top surface

During the induction brazing process, the melting of the Ag-Cu-Ti filler alloy is completely realized, dependent on the large quantities of heat and the elevated temperatures of the metallic wheel substrate. Previous literatures have reported that [27], when the heating temperature at the surface layer of AISI 1045 steel substrate arrives at 880–940 °C (especially at nearly 920 °C), good interfacial reaction could take place and strong joining is therefore formed among the CBN grains, Ag-Cu-Ti alloy and AISI 1045 steel in the vacuum furnace brazing process. For this reason, it is necessary to control the heating temperature of the wheel substrate surface ranged from 880 to 940 °C in the high-frequency induction brazing process.

2.3 Material properties and boundary conditions

The applied material properties (i.e., relative permeability, electrical resistivity, thermal conductivity, and volumetric heat capacity) are taken from the published literature [28–30] or provided by the manufacturers. The magnetic non-linearity and the dependence of physical properties on temperature are considered in the current finite element analysis.

The material properties of AISI 1045 steel are shown in Fig. 3. Particularly, some properties of the materials have been simplified for finite element stimulation. For example, the electrical resistivity and thermal conductivity of AISI 1045 steel is provided as the linear function with the independent variables of temperature, respectively, as follows:

$$\rho(T) = \rho_0(1 + \alpha_1 T) \tag{9}$$

$$\lambda(T) = \lambda_0(1 + \alpha_2 T) \tag{10}$$

where $\rho_0 = 1.3 \times 10^{-7}$ Ω·m is the electrical resistivity of AISI 1045 steel at 0 °C; $\alpha_1 = 8.8 \times 10^{-3}$ is the slope of the straight line expressed by Eq. (9); $\lambda_0 = 446$ W/(m·K) is the thermal conductivity of the wheel substrate at 0 °C; $\alpha_2 = -5.3 \times 10^{-4}$ is the slope of the straight line expressed by Eq. (10).

In FLUX finite element analysis software, the volumetric heat capacity of AISI 1045 steel can be achieved by the curve fitting as the superposition of the Gauss function and exponential function:

$$C_v = C_{vi} + (C_{v0} - C_{vi})e^{-\frac{T}{\tau}} + E \times \text{Gauss}(T) \tag{11}$$

$$\text{Gauss}(T) = \frac{1}{\sigma_0\sqrt{2\pi}} e^{-\frac{1}{2}\left(\frac{T-T_c}{\sigma_0}\right)^2} \tag{12}$$

where $C_{v0} = 3.5 \times 10^6$ J/(m^3·K) and $C_{vi} = 5.2 \times 10^6$ J/(m^3·K) indicate the volumetric heat capacity of AISI 1045 steel at 0 °C and ∞ °C, respectively; $E = 6.7 \times 10^8$ J/m^3 is the energy of phase transition of AISI 1045 steel. $\sigma_0 = 85$ is the Gaussian standard deviation, $T_c = 760$ °C is the temperature of phase transition, and $\tau = 400$ is the temperature coefficient.

In FLUX software, the magnetization curve (also named as B-H curve) of AISI 1045 steel can be described by series of straight lines of different slopes starting from the origin, as illustrated in Fig. 4. The B-H curves are expressed as follows:

$$B(H) = \mu_0 H + \mu_0(\mu_{r0} - 1)H \cdot \text{COEF}(T) \tag{13}$$

$$\text{COEF}(T) = \begin{cases} 1 - e^{\left(\frac{T-T_C}{C_0}\right)} & T < T_1 \\ e^{10\left(\frac{T_2-T}{C_0}\right)} & T > T_1 \end{cases} \tag{14}$$

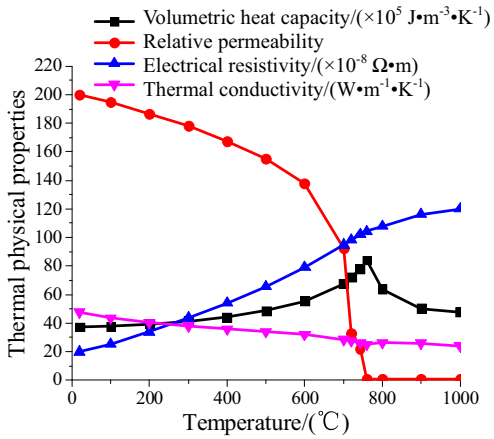

Fig. 3 Material properties of AISI 1045 steel

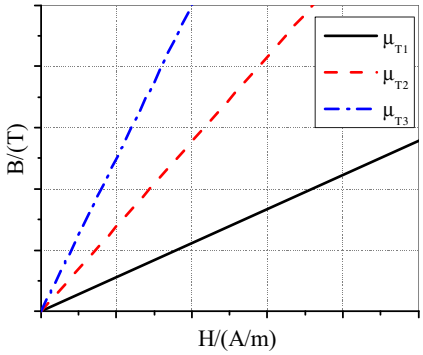

Fig. 4 Diagrammatic B-H curves of AISI 1045 steel

where $\mu_0 = 4\pi \times 10^{-7}$ H/m is the permeability of vacuum, $\mu_{r0} = 200$ is the initial relative permeability of AISI 1045 steel; COEF(T) is the temperature coefficient, in which $T_c = 760$ °C is the temperature of phase transition, $C_0 = 50$ is the temperature constant, and COEF(T_1) = 0.1.

The magnetizer is made up of Ferrotron 559H. Its magnetic properties (including flux density and the relative permeability) variation with the magnetic field strength is shown in Fig. 5, and the relative permeability can be approximated as a constant [31].

The thermal radiation and cross-ventilation are simulated for analysis: the environmental temperature is defined as 20 °C. The convective heat transfer coefficient and heat radiation coefficient between the brazing surface of the wheel and surrounding air are defined as 20 W/(m^2·K) and 0.5 W/(m^2·K^4), respectively.

2.4 Region selections for temperature distribution analysis

The temperature distribution obtained in induction heating is significantly influenced by four parameters as follows: current frequency, current magnitude, heating gap and scanning speed. Figure 6 displays the region selection for temperature distribution analysis in a quarter of the metallic wheel substrate. Point P is on the outer circumference of the wheel substrate below the inductor at the beginning of heating. Point A is also on the wheel outer circumference and the arc length l of PA is 90 mm. Two paths, denoted by I and II, are chosen in two different directions, shown as two red lines in Fig. 6. Path I is in the anticlockwise direction with the arc length of 40 mm, and the midpoint of path I is point A. Path II is also 40 mm in length, and starts from point A along the radius direction of the wheel.

2.5 Simulation process of temperature distribution

During the high-frequency induction brazing process, the temperature distribution characteristics at the effective heating zone are very important to form good joining among the CBN grains, Ag-Cu-Ti filler alloy, and metallic wheel substrate (i.e., AISI 1045 steel). Therefore, this article will primarily focus on investigating the temperature variation obtained at point A within the heating region. Based on the high-frequency induction heating technique, the brazing process could be described as follows:

(1) Adjust the distance (that is, the heating gap) between the inductor and the heating surface of the metallic wheel substrate.
(2) Load the electric current with a particular frequency and constant magnitude through the coil, and transfer the cooling water passing through the coil.
(3) Rotate the wheel in an anticlockwise direction at a constant speed (Fig. 1); in this case, the resultant heat and the elevated temperature of 880–940 °C could enable that the Ag-Cu-Ti filler alloy melts sufficiently to form good brazed joints between CBN grains and AISI 1045 wheel substrate. The Ag-Cu-Ti filler alloy melts merely within a narrow zone owing to the heating resulted from the heated wheel substrate of AISI 1045 steel.

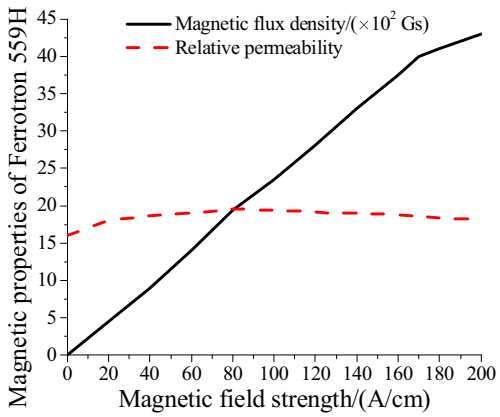

Fig. 5 Magnetic properties of Ferrotron 559H [16]

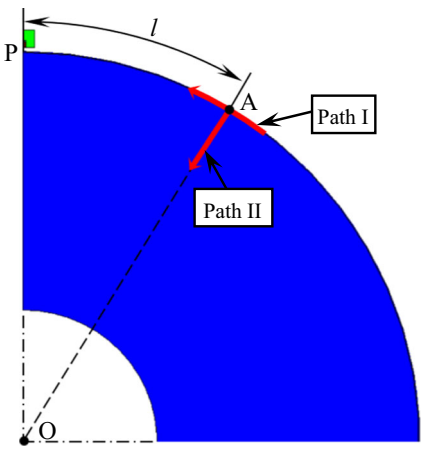

Fig. 6 Point A and two reference paths

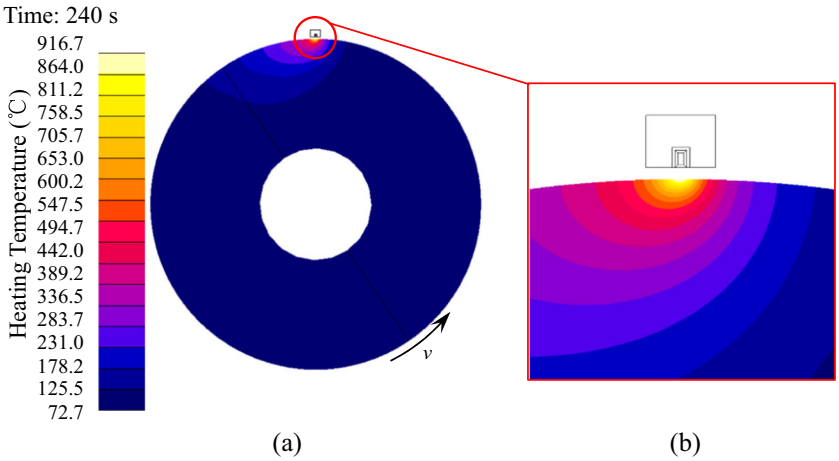

Fig. 7 Finite element simulation results of the typical temperature field. **a** Contour maps of typical temperature field at the heating zone. **b** Magnified view of the heating region

3 Results and discussion

3.1 Typical contour and evolution of temperature distribution in high-frequency induction heating

A typical contour of temperature distribution in the heating zone of the metallic wheel substrate is displayed in Fig. 7a. The heating gap between the inductor and wheel top surface is 2 mm and the wheel is rotated in an anticlockwise direction at the peripheral speed of 0.5 mm/s. Meanwhile, the alternating current is loaded in the coil with the magnitude of 20 A and high frequency of 1 MHz. The highest temperature obtained is 916 °C when the wheel substrate is heated for 240 s. The curve shown in Fig. 8a is obtained by calculating the highest temperature of the outer circumference of wheel substrate during the heating process. The heating procedure could be divided into two stages: the first is an initial temperature-rising stage (0–40 s), in which the temperature rises rapidly from 20 to 880 °C with the decreasing heating rate; the second is an effective heating stage (after 40 s), in which the highest temperature of wheel substrate increases from 880 °C, and reaches the temperature 916 °C at 180 s. The highest temperature keeps stable at 916 °C after 180 s, as the smooth part of the curve in Fig. 8a.

Figure 8b shows the change curve of resultant heating temperature at point A, which rotates following the wheel substrate during induction heating. The highest temperature is 916 °C at 180.4 s, while the displacement of point A is 90.2 mm. Obviously, Point A is 0.2 mm beyond the central coil in the scanning direction, and near the highest temperature point. Additionally, the highest temperature appears mainly at the heating region below the inductor, as shown in the contour maps of the heating region in Fig. 7b.

The temperature distribution along path I and II (shown in Fig. 6) at 180 s is demonstrated in Fig. 9, while the temperature of point A below the inductor is 914 °C and the highest temperature is 916 °C at the peak. As shown in Fig. 9a, point A is near the curve peak, and the temperature decreases quickly from the peak to the two ends of path I. At the same time, the temperature gradient in the positive direction of path I is slightly smaller compared with that in its negative direction. The lowest temperature is 880 °C at the 2-mm interval from 19.2 to 21.2 mm and reduced by merely 4 % compared with the highest value; however, the lowest temperature is 466 °C at the 10-mm interval from 15 to 25 mm and reduced by about 49 % compared with the highest one. Now it can be inferred that the effective heating region mainly concentrates at the 2-mm interval below the inductor.

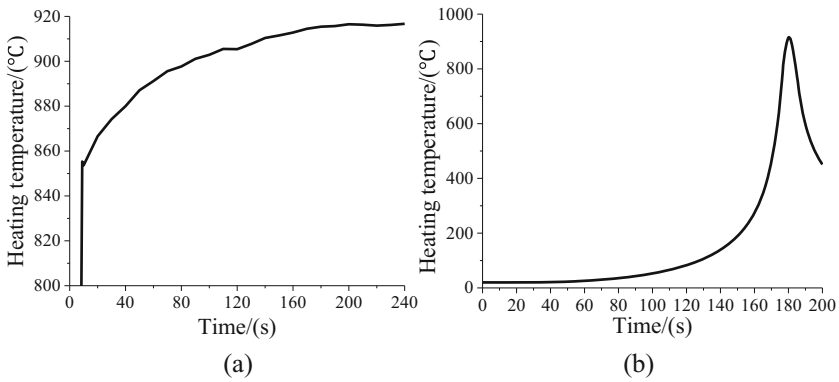

Fig. 8 Change curves of temperature during induction heating. **a** Time varying highest temperature curve in the wheel substrate **b** Change curve of temperature at point A

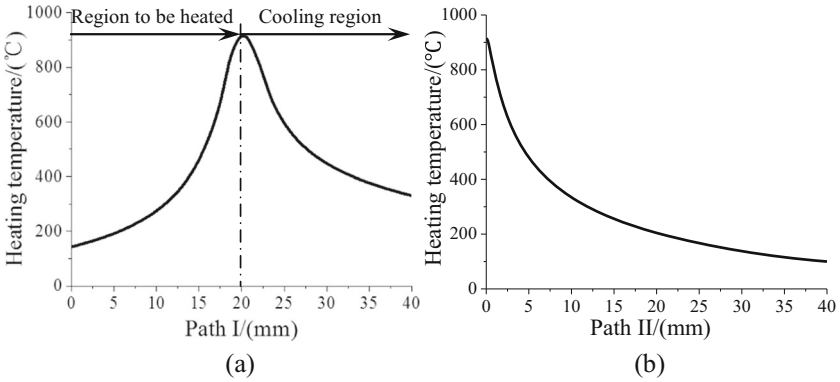

Fig. 9 Temperature distribution along two paths. **a** Along path I. **b** Along path II

The temperature distribution along path II is affected significantly by the skin effect during high-frequency induction heating. The eddy current is always generated on the top surface of the wheel substrate, and greatly focuses on the skin depth. Therefore, the region heated by the eddy current is shallow, and focuses on the top surface of the metallic wheel substrate. Figure 9b shows the temperature distribution along path II. The highest temperature, i.e., 914 °C, is obtained at point A (Fig. 6). Along the positive direction of path II, the temperature decreases rapidly from 0 (that is, the starting point A) to 10 mm, while the temperature gradient becomes smaller gradually from 10 to 40 mm. The temperature is 864 °C at the 0.55-mm position (equal to the skin depth), which is decreased by 6 % compared to that at point A. The temperature is 776 °C at the 1.1-mm position (twice the skin depth), which is decreased by 15 % compared to that at point A. The temperature is 652 °C at the 2.2-mm position (four times the skin depth), which is decreased by 29 % compared with that at Point A. Based on the above analysis, it is known that the depth of the dominating heating zone is equal to the skin depth on the top surface of wheel substrate.

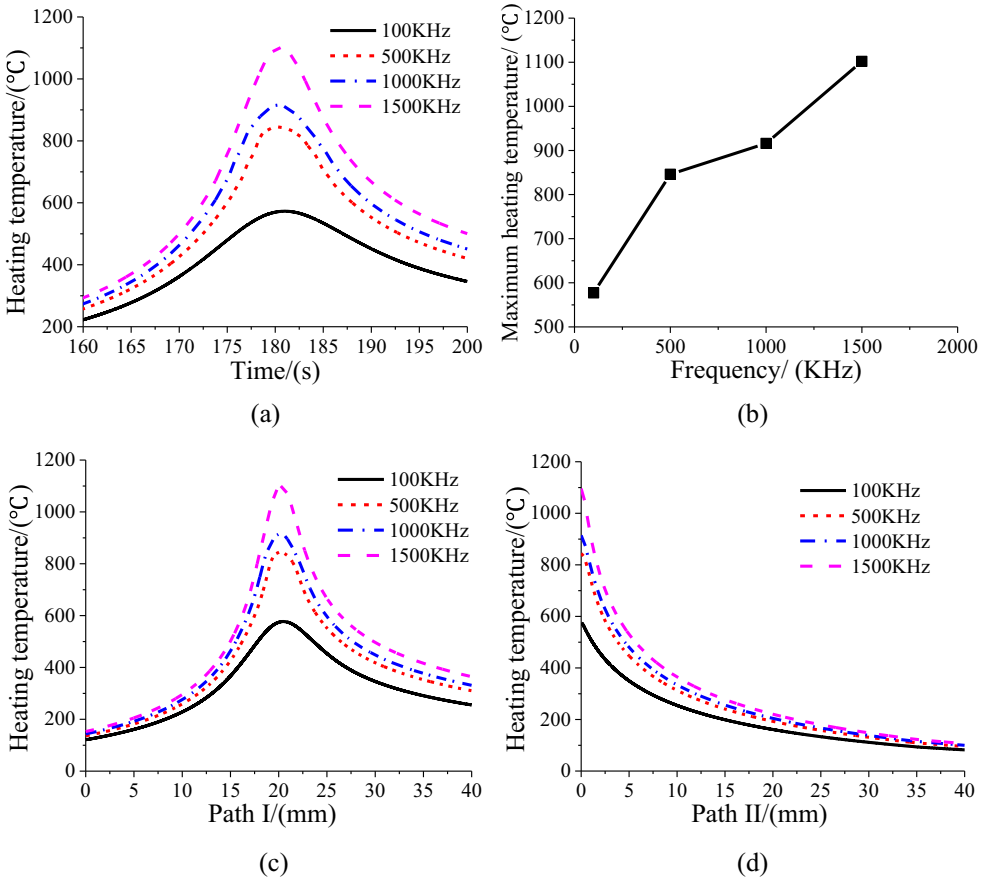

Fig. 10 Variation of temperature distribution versus current frequency. **a** Variation of heating curve. **b** Variation of highest temperature. **c** Temperature distribution along path I. **d** Temperature distribution along path II

3.2 Effects of high-frequency induction heating parameters on temperature distribution

3.2.1 Current frequency

In order to analyze the effects of the current frequency on the resultant temperature distribution, the other induction heating parameters are chosen as follows: the heating gap of 2 mm, the current magnitude of 20 A, and the peripheral scanning speed of 0.5 mm/s. The temperature curves of point A varying with the heating time are demonstrated in Fig. 10a. The resultant temperature of point A rises with an increasing heating rate, during which point A is rotated following the wheel substrate and approaches to the inductor gradually before 180 s. The temperature of point A is 914 °C when it is below the inductor at 180 s, while reaching the highest 916 °C at 180.4 s. Subsequently, point A rotates away from the coil, and the temperature of point A decreases gradually with a decreasing heating rate. Meanwhile, the heating rate and the highest temperature of point A increase with a higher frequency. When the heating time is 180 s, the highest temperature values of point A with different current frequencies are illustrated in Fig. 10b. The temperature is 914 °C with a current frequency of 1 MHz, which is decreased by 17 % in comparison to the temperature of 1096 °C with a current frequency of 1.5 MHz and increased by 8 % compared with the temperature of 844 °C with a current frequency of 500 KHz.

Figure 10c and d display the effects of the current frequency on the temperature distribution along path I and II, respectively. Obviously, the heating zone concentrates on the center more violently with a higher current frequency, which is more beneficial for increasing the heating rate and efficiency during the induction heating process. Considering that the temperature of 880–940 °C is essential for brazing CBN grains, the current frequency is optimized at 1 MHz.

3.2.2 Heating gap

The effects of the heating gap on the temperature distribution in induction heating are displayed in Fig. 11a. In this case, the peripheral scanning speed is 0.5 mm/s, the current is 20 A in magnitude and 1 MHz in frequency. It is significant that the heating rate and the highest temperature obtained at point A are increased with decreasing of the heating gap. Figure 11b shows that the temperature of point A is 819 °C when the heating gap is 3 mm, which is decreased by 11 % compared to 914 °C in case of the heating gap of 2 mm. The induction heating on the surface of the metallic wheel substrate is consumed to the surrounding environment by means of thermal radiation. The heat loss increases when the higher temperature

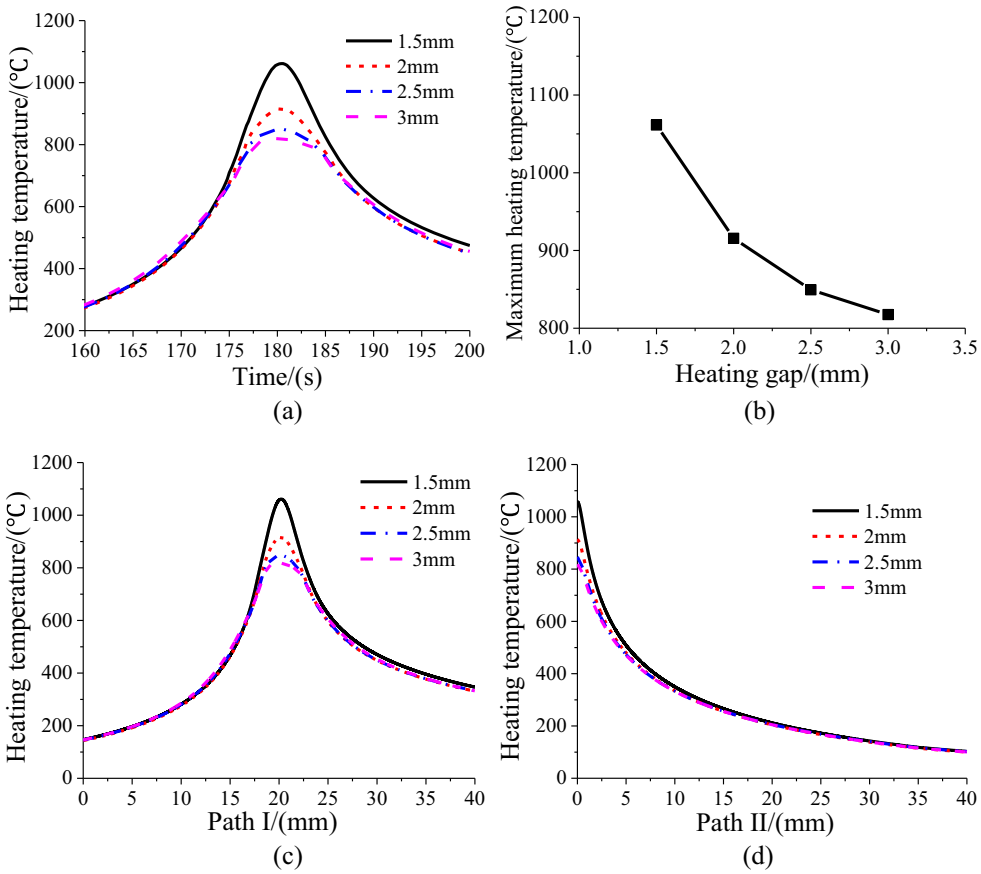

Fig. 11 Variation of temperature distribution versus heating gap. **a** Variation of temperature curve. **b** Variation of highest temperature. **c** Temperature distribution along path I. **d** Temperature distribution along path II

is obtained. Therefore, the highest temperature at point A is inversely proportional to the heating gap.

Figure 11c, d demonstrate the temperature distribution along path I and path II, respectively, versus the heating gap. When the heating gap value becomes smaller, the heating zone tends to concentrate on the central region of induction heating, and the rate and efficiency of induction heating become larger as well. Furthermore, the minimum heating gap is also required during induction brazing when taking into accounts the particle size of CBN grains (i.e., 150–400 μm) and the filler layer thickness (i.e., 60–160 μm), as displayed in Fig. 1b. As a result, heating gap of 2 mm is selected as the optimal parameter.

3.2.3 Current magnitude

On one hand, when the current magnitude increases, the inducted alternating magnetic field becomes stronger, which enlarges the eddy current generated on the metallic wheel substrate. On the other hand, larger induction heating current results in a higher heating power and heating rate. Figure 12a shows the effects of the current magnitude on the heating temperature of point A. The current frequency is 1 MHz with the heating gap of 2 mm, and the peripheral scanning speed is 0.5 mm/s. Figure 12a displays that both the highest temperature of point A and the heating rate increase with the larger current magnitude. Figure 12b demonstrates the highest temperature of point A versus different current magnitudes. The heating temperature is 849 °C in the case of an 18-A current, which is decreased by about 7 % compared with 914 °C in case of a 20-A current. Figure 12c, d both display that, when the current magnitude increases, the effective heating zone becomes thinner to the central area of induction heating, and the heating rate and efficiency get higher as well.

3.2.4 Scanning speed

The heating curves of point A at different scanning speeds are shown in Fig. 13a, in which 20-A current and 1-MHz frequency and 2-mm heating gap are applied. The heating time is 360.5, 180.4, 90.2, and 45.2 s, respectively, when the temperatures of point A reach the peak value at the different peripheral scanning speeds from 0.25 to 2 mm/s. According to the above facts, the distances of point A relative to the inductor could be calculated at the heating time mentioned above, and the distance is 0.125, 0.2, 0.2, and 0.4 mm, respectively, which are all much smaller than the inductor size of 12 mm and can be ignored. This implies that the scanning speed has little

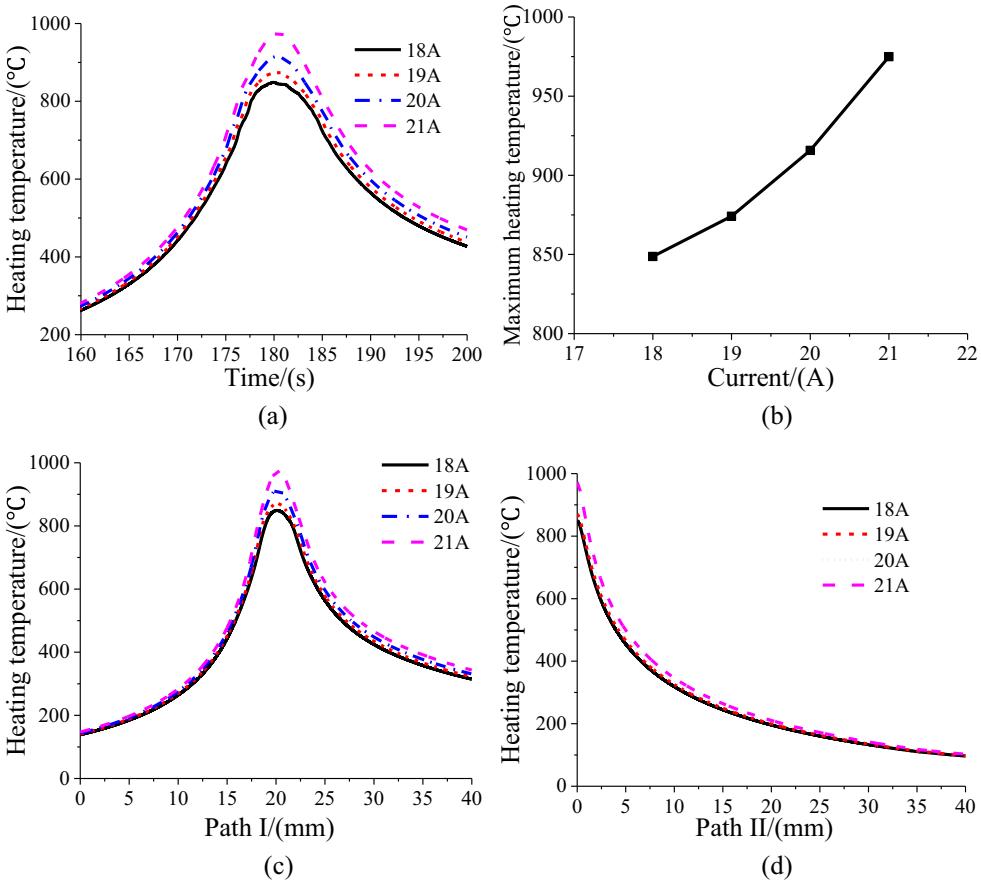

Fig. 12 Variation of temperature distribution versus current magnitude. **a** Variation of heating curve. **b** Variation of highest temperature. **c** Temperature distribution along path I. **d** Temperature distribution along path II

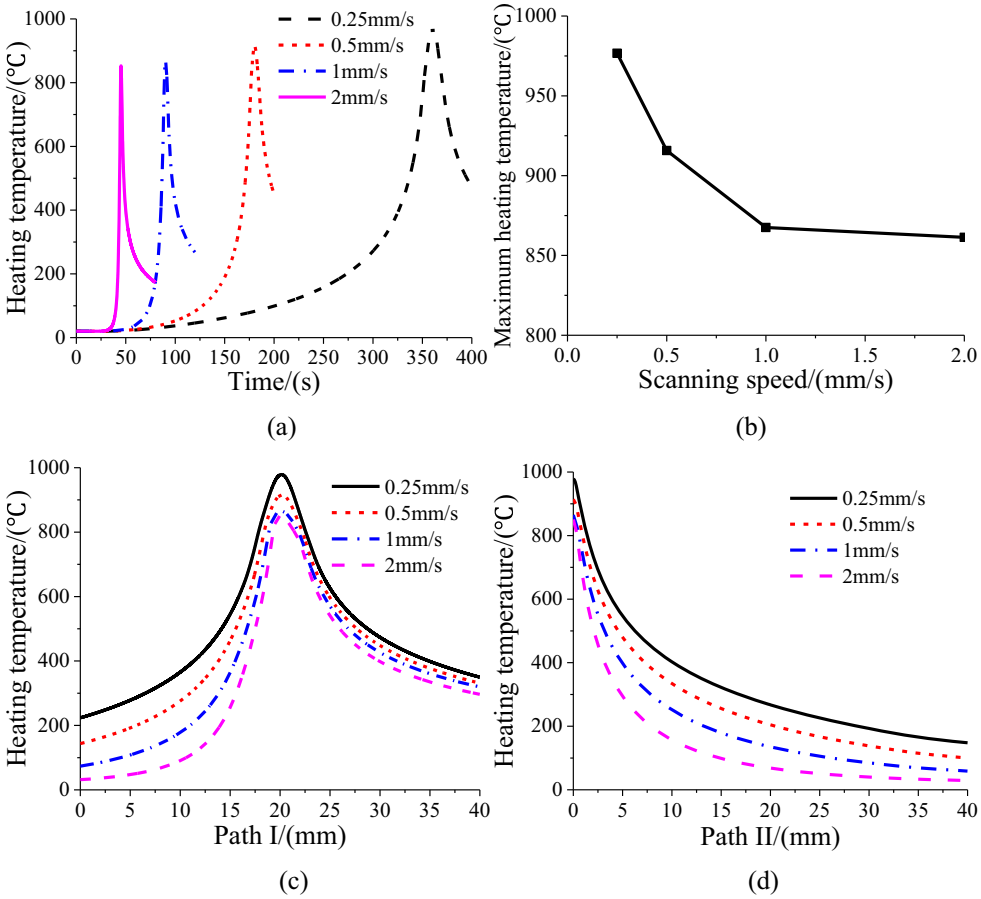

Fig. 13 Variation of temperature distribution versus peripheral scanning speed. **a** Variation of heating curve. **b** Variation of highest temperature. **c** Temperature distribution along path I. **d** Temperature distribution along path II

influence on the position where point A reaches the highest temperature. However, the highest temperature of point A is highly affected by the peripheral scanning speeds. As shown in Fig. 13b, the heating temperature is 977 °C in the case of the peripheral scanning speed of 0.25 mm/s, which is decreased by 6 % compared to 916 °C in case of the peripheral scanning speed of 0.5 mm/s. The heating temperature is 861 °C in case of the peripheral scanning speed of 2 mm/s, which is decreased by 6 % compared to 916 °C in case of the peripheral scanning speed of 0.5 mm/s. Higher peripheral scanning speed contributes to smaller heating temperature at the same position in the metallic wheel substrate.

When point A is rotated below the coil at 180 s, the temperature distributions along path I and II at different scanning speeds are provided in Fig. 13c, d, respectively. Point A is near the peak of the curve along path I, as shown in Fig. 13c. The region to be heated is on the left of the peak. It is obvious that the temperature distribution becomes more concentrated at higher scanning speed. The region on the right of the peak is the cooling region, in which the average temperature gradients of the curves are 31, 29, 27, and 28 °C/mm at different peripheral scanning speeds from 0.25 to 2 mm/s. It is obvious that the gradient values at different peripheral scanning speeds are approximately identical. Thus, the scanning speed nearly has no influence on the temperature distribution within the cooling part of the wheel substrate. Figure 13d displays the temperature distributions of point A along path II, and the curves are similar to those on the left part along path I from 0 to 20 mm. That is to say, the induction heating at a higher scanning speed would produce a higher temperature gradient, which makes the temperature distribution near point A much more inhomogeneous. When the scanning speed is lower, more time is provided to transfer the heat produced in the narrow central region below the coil to the surrounding regions in the wheel substrate. As such, the preheating effect of the region to be heated in the steel wheel substrate is more sufficient, and the temperature gradient becomes smaller at the lower scanning speed.

3.3 Experimental verification

In the brazing experiments of CBN grains, a high-frequency induction heating equipment modeled SPG-06AB III with a frequency of 1 MHz is used. The heating region of the CBN wheel and the inductor are in an argon atmosphere to prevent the oxidation. K-type thermocouple is applied to measure the heating temperature of point A, due to its suitable temperature

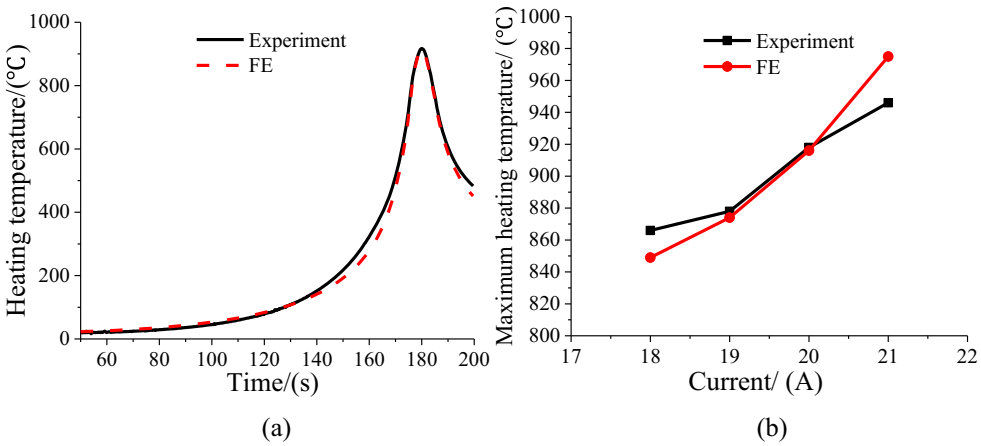

Fig. 14 Comparison of the heating temperature curves obtained in simulation and experiment. **a** Heating temperature curves of point A. **b** Highest temperatures varying with current magnitude

range (0–1300 °C), fine linearity, large thermo-electromotive force, high sensitivity, and strong resistance to oxidation.

3.3.1 Experimental verification of the heating curve and highest temperature of point A

The wheel substrate rotates and is heated. The distance between the temperature measuring point A and the inductor is 90 mm at the beginning of the heating, and point A is on the stable heating region based on the above analysis. In the brazing experiments, the heating gap between the inductor and the wheel substrate is adjusted to 2 mm, and the currents with different magnitudes are loaded on the both sides of the coil, and then the inductor scans through the heating surface of the metallic wheel substrate at a constant peripheral scanning speed of 0.5 mm/s until the inductor sweeps past point A and the temperature of the point begins to decrease.

The heating curves of point A obtained in both simulation and experiment are comparatively illustrated in Fig. 14a. At the initial heating stage (0–140 s), the simulated heating curve is essentially coincident with the experimental one; the temperature increases slowly in the two curves, and the highest temperature variation is 11 °C at 140 s. At the rapidly rising temperature stage (140–180 s), the temperature increases rapidly, and the heating rate obtained in the simulation work is always close to the experimental heating rate. The average value of the temperature variation between the simulation and the experiment is 29 °C, and the highest temperature variation is 48 °C at 162.6 s at this stage. At the cooling stage (after 180 s), the curves obtained in the simulation and the experiment are also nearly coincident.

The highest temperature varying with the current magnitude (18–21 A) in both the simulation and experiment is comparatively illustrated in Fig. 14b. When the current magnitude is 18 A, the temperature obtained in the simulation and experiment are 849 and 866 °C, respectively, which are 2 % in difference. When the current magnitude increases to 20 A, the temperatures in the simulation and experiment are 916 and 918 °C, and the difference between them is 0.2 %, which is the smallest one compared with those obtained with the other current magnitude. When the current magnitude increases to 21 A, the temperatures in the simulation and the experiment are 975 and 946 °C, respectively, which are 3 % in difference. Based on the above analysis, it is known that the difference of the highest temperature between simulation and experiment is less than 5 % with the different current magnitudes ranged from 18 to 21 A. That is to say, the simulation results are generally reasonable and accredited in the current work.

3.3.2 High-frequency induction brazing of CBN grains

Figure 15 displays the whole morphology of the brazed CBN grain, which is produced in the case of the optimum parameters as follows: heating gap of 2 mm, current frequency of 1 MHz, current magnitude of 20 A, and peripheral scanning speed of 0.5 mm/s. It is noted that, the polishing of brazed sample has been done to keep the three different layers (metallic wheel substrate, Ag-Cu-Ti filler alloy, and CBN grain) in

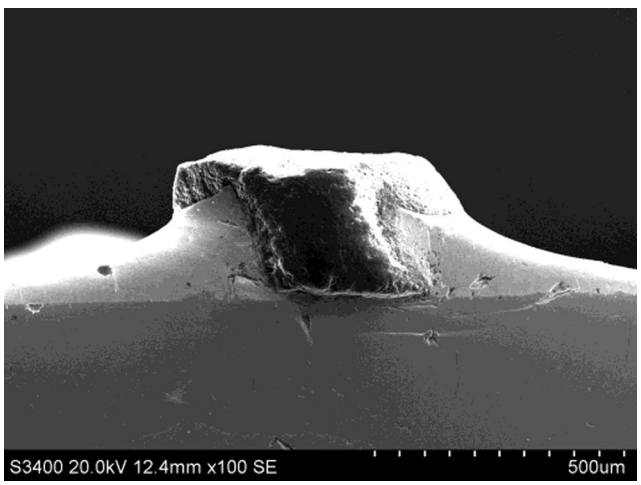

Fig. 15 Morphology of brazed CBN super-abrasive grain

a single plane; as such, the joining behavior of braze partners could be easily observed. In generally, a good brazing interface has been formed among the wheel substrate/Ag-Cu-Ti filler alloy/CBN grain when applying the abovementioned optimum parameters.

4 Conclusions

Temperature distribution and influencing factors in high-frequency induction brazing of CBN super-abrasive grains is researched based on finite element simulation. The following conclusions could be drawn:

(1) The effective heating zone with a width of 2 mm is concentrated on the top surface of metallic wheel substrate below the coil during the rotating induction heating process, and the depth of the dominating heating zone is equal to the skin depth (i.e., 0.55 mm).
(2) When heating at a higher current frequency, a higher current magnitude and a smaller heating gap values, the highest value of the resultant heating temperature becomes larger; however, a higher peripheral scanning speed makes the highest temperature decrease in the induction heating process.
(3) The optimum parameters for high-frequency inducting brazing of CBN grains are determined as the heating gap of 2 mm, current frequency of 1 MHz, current magnitude of 20 A, and peripheral scanning speed of 0.5 mm/s.
(4) The high-frequency induction brazing experiments of CBN grains has validated the simulation results, in which the errors of the highest temperatures between simulations and experiments are less than 5 %.

Acknowledgments The authors gratefully acknowledge the financial support for this work by the National Natural Science Foundation of China (No. 51235004 and No. 51375235), the Fundamental Research Funds for the Central Universities (No. NE2014103), the Science and Technology Support Program of Jiangsu Province (No. BE2013109), and the Foundation of Graduate Innovation Center in NUAA (No. YKFJJ20150506).

References

1. Bhaduri D, Kumar R, Jain AK, Chattopadhyay AK (2010) On tribological behaviour and application of TiN and MoS2-Ti composite coating for enhancing performance of monolayer cBN grinding wheel. Wear 268(9–10):1053–1065
2. Wang Y, Qiu XM, Sun DQ, Yin SQ (2011) Influence of Ti on microstructure and strength of c-BN/Cu-Ni-Sn-Ti composites. Int J Refract Met Hard Mater 29(2):293–297
3. Ding WF, Xu JH, Chen ZZ, Yang CY, Fu YC (2009) Microstructure characteristics of CBN/steel joints brazed with TiB2 modified active filler. Mater Sci Technol 25(12):1448–1452
4. Ay M, Caydas U, Hascalik A (2012) Optimization of micro-EDM drilling of Inconel 718 superalloy. Int J Adv Manuf Technol 66(5–8):1015–1023
5. Mao C, Zhang J, Huang Y, Zou HF, Huang XM, Zhou ZX (2013) Investigation on the effect of nanofluid parameters on MQL grinding. Mater Manuf Process 28:436–442
6. Ding WF, Xu JH, Chen ZZ, Su HH, Fu YC (2010) Grindability and surface integrity of cast Nickel-based superalloy in creep feed grinding with brazed CBN abrasive wheels. Chin J Aeronaut 23(4):501–510
7. Zhang YB, Li CH, Jia DZ, Zhang DK, Zhang XW (2015) Experimental evaluation of the lubrication performance of MoS_2/CNT nanofluid for minimal quantity lubrication in Ni-based alloy grinding. Int J Mach Tools Manuf 99:19–33
8. Zhang DK, Li CH, Zhang YB, Jia DZ, Zhang XW (2015) Experimental research on the energy ratio coefficient and specific grinding energy in nanoparticle jet MQL grinding. Int J Adv Manuf Technol 78:1275–1288
9. Mao C, Zou HF, Zhou X, Huang Y, Gan HY, Zhou ZX (2014) Analysis of suspension stability for nanofluid applied in minimum quantity lubricant grinding. Int J Adv Manuf Technol 71:2073–2081
10. Azizi A, Rezaei SM, Rahimi A (2010) Study on the rotary cup dressing of CBN grinding wheel and the grinding performance. Int J Adv Manuf Technol 47(9–12):1053–1063
11. Ding WF, Xu JH, Chen ZZ, Su HH, Fu YC (2011) Brazed joints of CBN grains and AISI 1045 steel with AgCuTi-TiC mixed powder as filler materials. Int J Miner Metall Mater 18(6):717–724
12. Ma B, Zhu H (2015) Study on induction brazing of diamond grits coated by physical vapor deposition. Int J Adv Manuf Technol 80:599–605
13. Zhang LX, Feng JC, Liu HB (2008) High frequency induction brazing of TiC cermets to steel with Ag-Cu-Zn foil. Mater Sci Technol 24(5):623–626
14. Li QL, Xu JH, Su HH, Lei WN (2015) Fabrication and performance of monolayer brazed CBN wheel for high-speed grinding of superalloy. Int J Adv Manuf Technol 80:1173–1180
15. Codrington J, Nguyen P, Ho SY, Kotousov A (2009) Induction heating apparatus for high temperature testing of thermo-mechanical properties. Appl Therm Eng 29:2783–2789
16. Jang JY, Chiu YW (2007) Numerical and experimental thermal analysis for a metallic hollow cylinder subjected to step-wise electro-magnetic induction heating. Appl Therm Eng 27:1883–1894
17. Franco C, Acero J, Alonso R, Sagüés C, Paesa D (2012) Inductive sensor for temperature measurement in induction heating applications. IEEE Sensors J 12(5):996–1003
18. Chen QS, Gao P, Hu WR (2004) Effects of induction heating on temperature distribution and growth rate in large-size SiC growth system. J Cryst Growth 266:320–326
19. Mei RB, Li CS, Liu XH, Li B, Han B (2011) Modeling of slab induction heating in hot rolling by FEM. Engineering 3:364–370
20. Zhang ZY, Yang H, Li H, Tao Z, Wang D (2014) Thermo-mechanical coupled 3D-FE modeling of heat rotary draw bending for large-diameter thin-walled CP-Ti tube. Int J Adv Manuf Technol 72(9–12):1187–1203
21. Chen SC, Peng HS, Chang JA, Jong WR. Rapid mold surface heating/cooling using electromagnetic induction technology. International Conference on Mechatronics. July 10–12, 2005, Taipei, Taiwan
22. Keer RV, Dupré LR, Melkebeek JAA (1996) On a numerical method for 2D magnetic field computations in a lamination with enforced total flux. J Comput Appl Math 72:179–191
23. Zhu TX, Li XK, Li F, Rong Y. The establishment of coupled electromagnetic-thermal analytical model of induction heating system with magnetic flux concentrator and the study on the effect of

magnetic permeability to the modeling. ASME International Manufacturing Science and Engineering Conference. June 10–14, 2013, Madison, Wisconsin, USA
24. Eastwood MD, Haapala KR (2015) An induction hardening process model to assist sustainability assessment of a steel bevel gear. Int J Adv Manuf Technol 80(5–8):1–13
25. Nemkov V, Goldstein R (2003) Computer simulation for fundamental study and practical solutions to induction heating problems. Compel Int J Comput Math Electr Electron Eng 22(1):181–191
26. Rudnev V, Loveless D, Cook RL, Black M (2003) Handbook of induction heat. Marcel Dekker, New York
27. Ding WF, Xu JH, Chen ZZ, Su HH, Fu YC (2010) Effects of heating temperature on interfacial microstructure and compressive strength of brazed CBN-AlN composite abrasive grits. J Wuhan Univ Technol-Mater Ed 25(6):952–956
28. Arita H, Todaka T, Enokizono M (2002) Thermal magnetic characteristic for high frequency induction heating analysis. J Appl Phys 91(10):8317–8318
29. Shen B, Song B, Cheng L, Lei XL, Sun FH (2014) Optimization on the HFCVD setup for the mass-production of diamond-coated micro-tools based on the FVM temperature simulation. Surf Coat Technol 253:123–131
30. Norouzifard V, Hamedi M (2014) A three-dimensional heat conduction inverse procedure to investigate tool–chip thermal interaction in machining process. Int J Adv Manuf Technol 74(9–12): 1637–1648
31. Li F, Li XK, Zhu TX, Rong Y. Numerical simulation of the moving induction heating process with magnetic flux concentrator. Advances in Mechanical Engineering, 2013, Article ID 907295 (9 pages)